Ab initio investigation on exciton-phonon interaction and exciton mobility in black phosphorene

Xirui Tian,[1] Qijing Zheng,[1] Xiang Jiang [1,*] and Jin Zhao [1,2,†]

[1]*Department of Physics and ICQD/Hefei National Research Center for Physical Sciences at the Microscale, and Synergetic Innovation Center of Quantum Information & Quantum Physics, University of Science and Technology of China, Hefei, Anhui 230026, China*
[2]*Department of Physics and Astronomy, University of Pittsburgh, Pittsburgh, Pennsylvania 15260, USA*

Black phosphorene (BP) is an emerging two-dimensional material that has potentially wide applications in nano- and optoelectronics. Despite the strong excitonic effects observed in few-layer BP, there is still a lack of understanding regarding exciton-phonon (*ex-ph*) interaction and exciton mobility. In this work, using *GW* plus real-time Bethe-Salpeter equation approach, it is revealed that the out-of-plane acoustic phonon mode *ZA*, and the optical phonon modes A_g^1 and A_g^2 couple strongly with the exciton. Among them, the A_g^2 mode has a uniquely significant influence on the oscillator strength. Driven by these *ex-ph* interactions, the exciton becomes more localized accompanied with strengthened binding and the absorption spectrum undergoes a notable renormalization at 300 K. In the framework of deformation potential theory, the exciton mobility of monolayer BP (MLBP) is found to be largely suppressed compared to the free-charge carriers, showing quasi-one-dimensional character. This work provides rich knowledge of *ex-ph* interaction and exciton mobility in MLBP at the *ab initio* level, offering insights for the understanding and controlling the exciton behavior in BP-based devices.

I. INTRODUCTION

Layered black phosphorus, or black phosphorene (BP), as a novel category of two-dimensional (2D) semiconductors, has been demonstrated having various remarkable properties—widely tunable direct band gap, anisotropy, and high carrier mobility, showing great potential in the area of optoelectronics [1–11]. Specifically, the direct band gap of BP varies from 0.3 eV in bulk to 2.0 eV in monolayer, covering the visible and near-infrared range in spectrum and filling up the blank between gapless graphene and large-gap transition-metal dichalcogenides [2–5]. Its puckered honeycomb structure gives rise to distinctly anisotropic electronic and optical properties, enabling the applications that are impossible in isotropic materials [6–10]. And, its exceptional carrier mobility ensures the performance of BP-based devices such as field-effect transistor and photovoltaics [8,11].

Phonon is general existing elementary excitation in solid materials and the electron-phonon (*e-ph*) interaction is known to be a key ingredient that affects the optical, electronic, and thermal behavior of carriers in semiconductor devices [8, 12–21]. Especially, the electronic structure of BP is sensitive to structural distortion, suggesting a strong *e-ph* interaction [12,13]. Due to its basic importance, the *e-ph* interaction in BP has been extensively studied by both experimental and theoretical works. Experimental researches have observed symmetry-dependent e-*ph* coupling by polarization-selective

resonance Raman measurements [14]. On the theoretical side, *ab initio* investigations have been applied to study the *e-ph* coupling in BP, which can be divided into three catagories: (i) perturbation theory [15,16]; (ii) statistical sampling over *ab initio* molecular dynamics (AIMD) [17–21]; and (iii) deformation potential theory [8].

However, all these previous *ab initio* studies have been established on the single-particle picture where the essential excitonic effect in 2D materials is in absence. The most recognized *ab initio* approach to investigate exciton properties is the *GW* + Bethe-Salpeter equation (*GW* + BSE) method. Using this approach, it has been revealed that exciton binding energy in monolayer BP (MLBP) is as large as $0.5 \sim 0.9$ eV [3,9,22] as confirmed by spectroscopy experiments [10]. Such a robust binding renders the performance of devices greatly subjected to the behavior of exciton in MLBP [23–25]. It is fundamental to study the exciton-phonon (*ex-ph*) interaction with many-body effects taken into account. Up to now very few studies related to *ex-ph* interaction have been reported due to the boost of complexity. Zacharias and Giustino introduced the special displacement method to construct the structure that yields the thermodynamic average at finite temperature [26] and studied the effects of *ex-ph* coupling on monolayer germanium selenide [27]. Chen *et al.* derived the *ex-ph* coupling matrix elements within the BSE framework [28], facilitating understanding of *ex-ph* coupling based on perturbation theory combined with *GW* + BSE. And recently, Jiang *et al.* developed an *ab initio* method on the basis of *GW* plus the real-time BSE (*GW* + rtBSE) [29], in which *GW* + BSE is combined with AIMD by introducing the rigid dielectric function approximation, making it affordable to obtain the time-varying properties of exciton along an AIMD

_____

*jxiang@mail.ustc.edu.cn
†zhaojin@ustc.edu.cn

trajectory which contains extensive information about *ex-ph* interaction at a picosecond (ps) timescale, providing another efficient way to investigate *ex-ph* interaction at the *ab initio* level.

In this paper, we study the *ex-ph* interaction in MLBP utilizing GW + rtBSE simulation. A 5-ps AIMD trajectory of MLBP at 300 K simultaneously containing phonon excitation and many-body effects is generated. Through frequency spectral analysis we identify that the out-of-plane acoustic phonon mode *ZA*, and the optical phonon modes A_g^1 and A_g^2 couple strongly with the exciton in MLBP and elucidate their impact on energy and oscillator strength. Through ensemble average we determine the increase of exciton binding energy aligned with wave-function localization, and show the renormalization of optical response due to phonon excitation. Besides, we calculate the acoustic phonon limited exciton mobility based on deformation potential theory, which quantifies the huge lowering of mobility when the independent electron and hole are bound together to form an exciton and demonstrates the quasi-1D character of exciton transport in MLBP.

II. METHODS

The AIMD simulation of MLBP is calculated by employing density-functional theory (DFT) using Vienna *Ab initio* Simulation Package (VASP) [30]. A 20-Å vacuum layer is introduced to avoid the spurious interaction between the periodic images. The plane-wave cutoff energy is set as 400 eV. A $6 \times 6 \times 1$ supercell with $3 \times 3 \times 1$ *k* points is used to capture the effects of sufficient phonon modes. The exchange-correlation interaction is described by the Perdew-Burke-Ernzerhof (PBE) functional [31]. We heat the system to 300 K through Nosé-Hoover heat bath [32] and obtain a 5-ps AIMD trajectory under the microcanonical ensemble with a 1-fs time step. Subsequently, in order to reduce the computation cost, we choose a 5-fs time step for the real-time BSE calculation. The time step is small enough considering that the maximum phonon frequency in MLBP is about $460 \, \text{cm}^{-1}$ (~ 72 fs) [16].

The GW + rtBSE workflow is implemented in HEFEI-NAMD code [29]. A single-point GW calculation of unit cell with $18 \times 18 \times 1$ *k* points is carried out using VASP to provide the quasiparticle (QP) energy and the dielectric response within the random-phase approximation (RPA). The band-gap difference between the single-point GW and the DFT result is used to correct the underestimated Kohn-Sham (KS) energies during the AIMD. For an accurate description of energy levels, partially self-consistent GW (G_1W_0) is performed where the QP energies are iteratively updated from the one-shot GW (G_0W_0). Then, the BSE Hamiltonian is constructed using seven conduction bands and three valence bands of the supercell and solved for each time step along the AIMD trajectory based on rigid dielectric function approximation that the dielectric function and QP energy correction are fixed along the AIMD trajectory on account of their ignorable effect compared to the variation of wave function [28,33]. More details related to the method can be found in the Supplemental Material [34].

III. RESULTS AND DISCUSSION

A. Band structure and exciton properties of MLBP at zero temperature

Before studying *ex-ph* interaction, we first examine the band structure and exciton properties of MLBP at zero temperature. The band structure of MLBP is given in Fig. 1(b). DFT calculation with PBE functional gives a direct band gap of 0.89 eV at the Γ point, which is underestimated due to the well-known self-interaction error [3,9,22]. For a correction, GW calculation is performed to obtain the QP energies, resulting in a band gap of 2.06 eV. Comparing the band structure of DFT and GW calculations, the self-energy correction can be understood as a rigid shift of KS energy bands. This energy shift of 1.17 eV is used as a scissor operator to modify the QP energies during the AIMD simulation.

After photoexcitation, the strong Coulomb attraction between electron and hole leads to the formation of exciton in MLBP which significantly affects the optical response. Generally, the characteristic of exciton can be captured by GW + BSE calculation. The polarized absorption spectra of MLBP in equilibrium at zero temperature is given in Fig. 1(c). For armchair (AR) polarization the lowest bright exciton peak appears at 1.49 eV (labeled as A). Comparing the GW + BSE spectra with GW + RPA spectra, the binding energy for A exciton is determined to be 0.57 eV, which is in good consistence with previous calculations [3,9,22]. By contrast, for zigzag (ZZ) polarization the first bright exciton peak (labeled as B) does not appear until reaching 3.0 eV. A exciton, closely related to the band-edge transition, plays a dominant role in MLBP. Therefore, we focus on the interaction between A exciton and phonon in this study.

B. Phonon effects on the QP and exciton energies

The time evolution of QP energies at 300 K is presented in Fig. 2(a). First, we investigate the *e-ph* coupling of the independent electron and hole by performing Fourier transform (FT) on the energy evolution of conduction-band minimum (CBM) and valence-band maximum (VBM). In the subsequent FT spectra [Fig. 2(b)], there are four major peaks. The two low-frequency peaks originate from the *ZA* mode and the two high-frequency peaks are, respectively, assigned to A_g^1 and A_g^2 optical modes by comparing them with theoretical results [17] and Raman-scattering measurements [7,14]. B_{2g} mode also plays a minor role. Since the frequencies of B_{2g} ($425 \, \text{cm}^{-1}$) and A_g^2 ($448 \, \text{cm}^{-1}$) modes come very close to each other, and the duration of MD is not long enough for us to distinguish them, we identify the B_{2g} mode at its second-harmonic peak in the FT spectra. It is found that most of the phonon modes simultaneously lift up CBM and lower down VBM, or vice versa, suggesting the effects of phonon scattering on the CBM electron and the VBM hole have the opposite phases. Therefore, comparing the sum of FT of CBM and VBM with the FT of band gap, a great identity is observed [Fig. 2(b)]. Such opposite phases are supposed to give rise to a maximum augmentation of phonon scattering when electron and hole binds together to form an exciton.

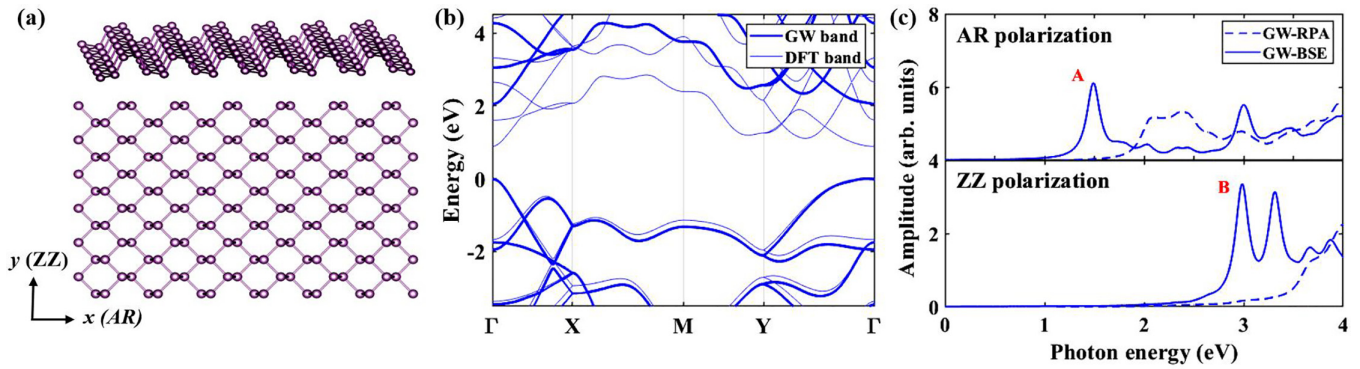Then we turn to the exciton case. The time evolution of the CBM-VBM band gap and A exciton at 300 K is

FIG. 1. (a) Atomic structure of MLBP. (b) *GW* (thick lines) and DFT bands (thin lines) of MLBP. (c) Polarized absorption spectra of MLBP in equilibrium from *GW*-RPA without *e-h* interaction (dashed lines) and *GW*-BSE with *e-h* interaction (solid lines) under AR direction (top) and ZZ direction (bottom) polarized light.

presented in Fig. 2(c). The corresponding averaged values are, respectively, 2.01 and 1.42 eV. Comparing to the results at zero temperature, the band gap decreases by 48 meV due to the *e-ph* induced renormalization [35]. The average binding energy of *A* exciton increases by 20 meV to 0.59 eV at 300 K with *ex-ph* coupling included. The FT spectra of *A* exciton resembles that of the band gap, which is attributed to the narrow distribution of *A* exciton in the momentum space revealed by the modular square of exciton wave-function coefficient

$|A_{kcv}|^2$ (see Supplemental Material, Fig. S3 [34]), suggesting *A* exciton is composed by electronic states around CBM and VBM. And, the slight difference comes from the renormalization of exciton binding energy induced by phonons.

C. Phonon-induced exciton localization

Thermal vibrations of lattice, namely, the phonon excitation, introduce disorder in the material that generally causes
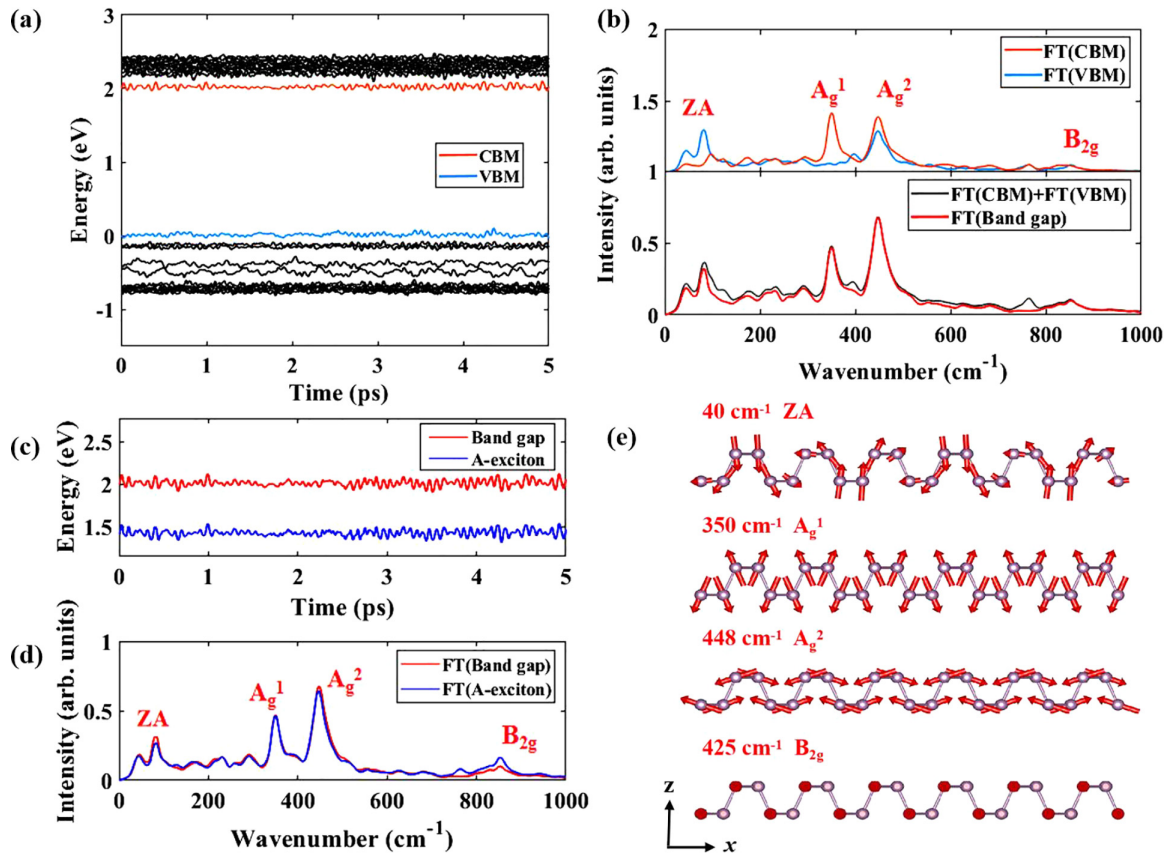

FIG. 2. (a) Time evolution of KS electronic-state energies of MLBP. (b) Top: FT spectra of evolution of VBM and CBM. Bottom: comparison between sum of FT spectra of CBM and VBM and FT spectrum of band gap. (c) Time evolution of band gap and energy of *A* exciton. (d) FT spectra of evolution of band gap and *A* exciton. (e) Corresponding frequencies and vibrational schematic diagrams of phonon modes appearing in FT spectra.
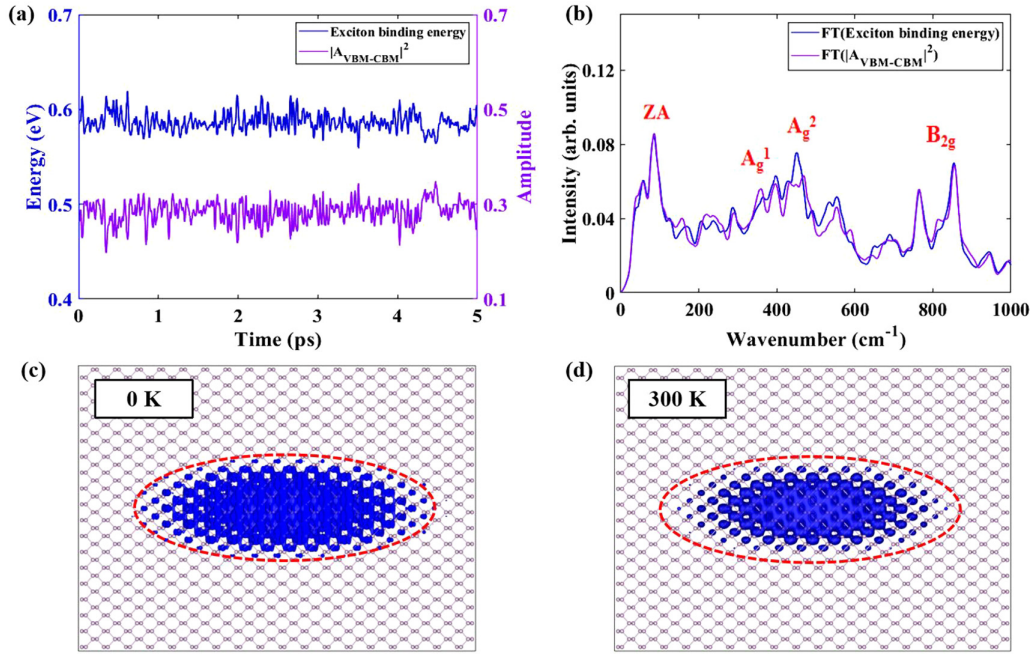
FIG. 3. (a) Time evolution of binding energy and $|A_{CBM-VBM}|^2$ of A exciton. (b) FT spectra of A-exciton binding energy and $|A_{CBM-VBM}|^2$. Amplitudes of two FT spectra have been normalized to same level. (c), (d) Modulus squared of the real-space A-exciton wave function at 0 K (c) and averaged over AIMD trajectory at 300 K (d). Rectangle frame corresponds to size of $18 \times 18 \times 1$ supercell. Two dotted ellipses in (c) and (d) both refer to outline of A exciton at zero temperature. And, isosurfaces in (c) and (d) are plotted using same value.

charge localization in real space [36–38]. One may expect that phonon excitation may also induce exciton localization in MLBP. The exciton localization can be revealed in both real and momentum space. The centralization of A exciton in the momentum space can be understood from the square of its wave-function coefficient at Γ point $|A_{CBM-VBM}|^2$. In Fig. 3(a) we plot the time evolution of $|A_{CBM-VBM}|^2$, together with the binding energy of A exciton. The time-resolved trajectories of the binding energy and $|A_{CBM-VBM}|^2$ are found similar in shape but opposite in changing trend, and their FT spectra are in line with each other [Fig. 3(b)], suggesting $|A_{CBM-VBM}|^2$ is negatively correlated with the binding energy. The increase of A-exciton binding energy due to *ex-ph* coupling is accompanied with a more delocalized distribution in the momentum space, which corresponds to a localization in the real space.

The phonon-induced exciton localization can also be understood directly from the modulus squared of the real-space exciton wave function with the hole coordinates being integrated out, i.e., $\rho_\lambda(\mathbf{r}) = \int d\mathbf{r}_h |\psi_\lambda(\mathbf{r}_e = \mathbf{r} + \mathbf{r}_h, \; \mathbf{r}_h)|^2$ [39]. The effects of phonon excitation are included by averaging over the *NVE* ensemble from AIMD. The real-space distribution of A exciton displays a $1s$ hydrogen-like elliptical envelope that mainly extends in the AR direction as plotted in Fig. 3(c) and 3(d). The two dashed ellipses in Figs. 3(c)–3(d) are both the outline of A exciton at zero temperature and the two isosurfaces are plotted using the same amplitude. It is clear that the exciton size is reduced when the temperature increases from zero temperature to 300 K. To further quantitatively evaluate the localization of exciton, we calculate the size of A exciton using $\bar{r} = \int d\mathbf{r} |\mathbf{r}| \rho_\lambda(\mathbf{r})$. The values are, respectively, 12.56 Å at zero temperature and 12.35 Å at 300 K. Such a 0.21-Å decrease illustrates that the average distance between *e-h* pair

is compressed and the exciton binding is strengthened when phonons are excited, well consistent with the 20-meV increase of the exciton binding energy.

D. Exciton-phonon effects on the optical response

To understand the *ex-ph* effects on the optical response, we calculate the exciton oscillator strength defined as [40]

$$T_\lambda = \frac{|\langle 0|\vec{v}|\lambda\rangle|^2}{E_\lambda} = \frac{\left|\sum_{kcv} A_{kcv}^\lambda \langle ck|\vec{v}|vk\rangle\right|^2}{E_\lambda}. \quad (1)$$

$|0\rangle$ denotes the ground state. Using the velocity-coordinate commutation relation $\vec{v} = i[H, \; \vec{r}]$, $\langle ck|\vec{v}|vk\rangle$ can be rewritten as $\langle ck|\vec{v}|vk\rangle = i(E_{kc} - E_{kv})\langle ck|\vec{r}|vk\rangle$, where E_{kc} and E_{kv} are the QP energies and $\langle ck|\vec{r}|vk\rangle$ is the transition dipole matrix element. On account of the nonperiodicity of $\vec{r}$, $\langle ck|\vec{r}|vk\rangle$ is converted to $\lim_{q\to 0} \frac{1}{|q|}\langle ck|e^{i\vec{q}\cdot\vec{r}}|vk\rangle$ in practice, where $\vec{q}$ is the wave vector of the incident light. The calculation of such matrix element is implemented in VASP as explained in Ref. [41].

Figure 4(a) shows the relative change of modular square of the transition dipole from VBM to CBM ($|\langle CBM|\vec{r}|VBM\rangle|^2$) corresponding to the equilibrium structure. In its FT spectrum [Fig. 4(b)], A_g^1 and A_g^2 modes contribute two major peaks, with A_g^2 being the strongest. By further incorporating the contribution from the exciton energy and wave-function coefficients according to Eq. (1), the time-varying oscillator strength of A exciton and its FT spectrum are shown in Figs. 4(c) and 4(d). Notably, the coupling amplitudes of *ZA* and B_{2g} modes are enhanced due to the excitonic effects. Yet, A_g^2 still remains the strongest phonon mode coupled to the oscillator strength. The phonon excitation reduces both the transition
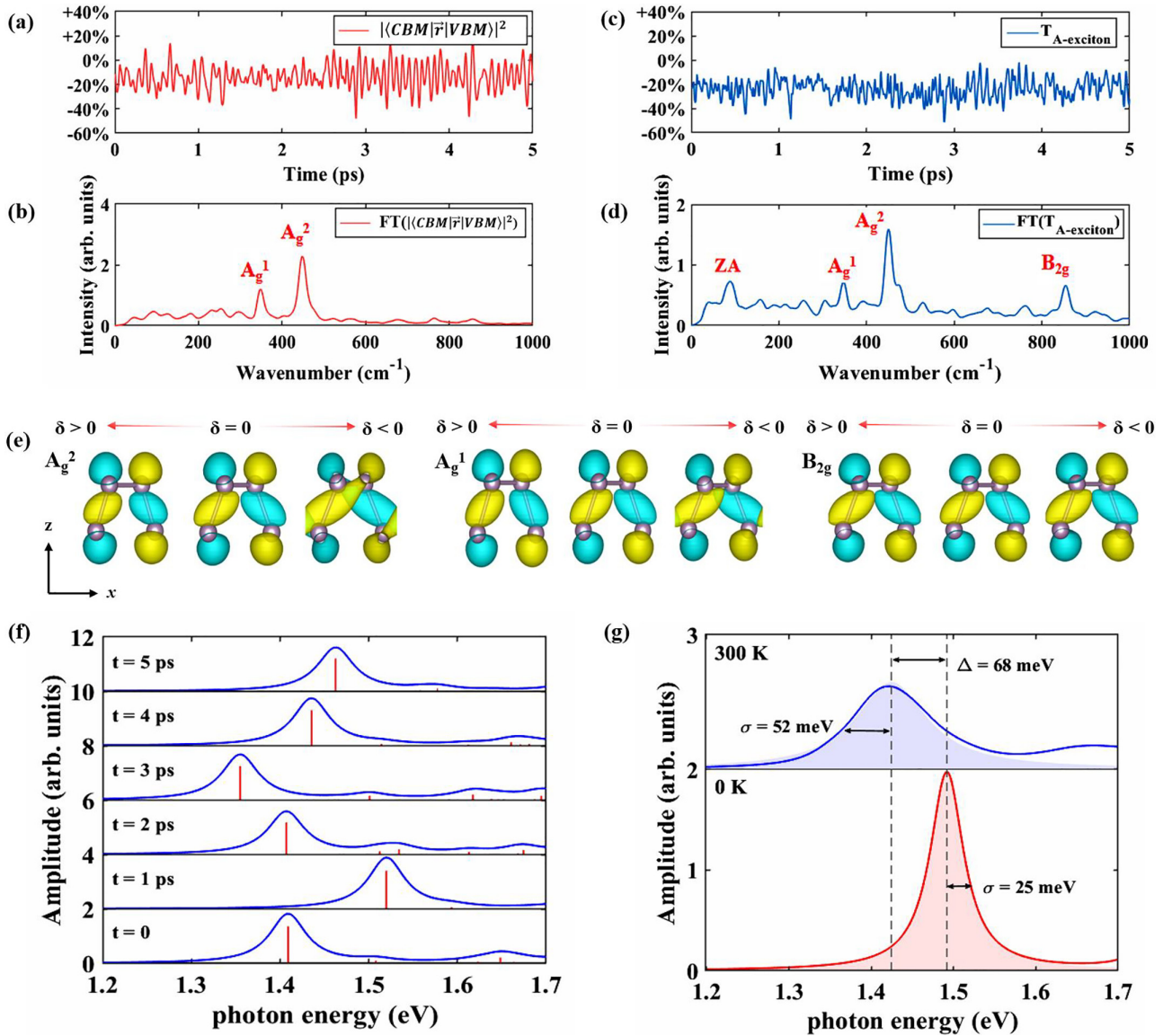
FIG. 4. (a), (b) Time evolution of square of transition dipole moment from VBM to CBM $|\langle CBM|\vec{r}|VBM\rangle|^2$ and corresponding FT spectrum. (c), (d) Time evolution of oscillator strength of A exciton and corresponding FT spectrum. Y-axis coordinates in (a) and (c) denote relative change of square of transient transition dipole or exciton oscillator strength compared to result of equilibrium structure. (e) VBM orbital distribution variations with A_g^2, A_g^1, and B_{2g} phonon mode excitation. To display variation clearly, we introduce considerably large displacement ($\delta = \pm 0.3$ Å within primitive cell). $\delta = 0$ refers to equilibrium structure. $\delta > 0$ and $\delta < 0$ suggest atomic displacements aligned to two opposite phonon vibrational directions. (f) Six different snapshots of absorption spectra along AIMD trajectory. Red lines denote exciton oscillator strengths. (g) Top: Averaged absorption spectrum of AIMD ensemble at 300 K. Bottom: Absorption spectrum at zero temperature. Shaded areas are fitted Lorentz functions of first peak.

dipole moment and the oscillator strength of A exciton, which decrease around 14% and 24%, respectively, comparing to the equilibrium structure.

The extraordinary tuning effects of A_g modes (A_g^1 and A_g^2) on the transition dipole moment $|\langle CBM|\vec{r}|VBM\rangle|^2$ can be explained by checking how the phonon excitation affects the orbital distribution. The impacts of phonon excitation on the CBM are not distinct (see Supplemental Material, Fig. S4 [34]) and the leading effects are on the VBM. In Fig. 4(e) we plot how the VBM orbital changes when A_g^1, A_g^2, and B_{2g} modes are excited by introducing a considerably large atomic displacement—the total displacement within a primitive cell

is set to be $\delta = \pm 0.3$ Å for each phonon-activated structure. One can see that the excitation of A_g modes alters the VBM orbital distribution much more notably than B_{2g} mode by compressing or stretching the σ bonds that connect two P-atom sublayers. Besides, the σ bond primarily extends along the AR direction, thus more susceptible to A_g^2 mode with a larger AR vibrational component. This result agrees with the polarized Raman measurements revealing the strong *e-ph* coupling of the in-plane atomic movements from A_g^2 mode vibration [14]. It should be noted that due to the phonon excitation, the xz−mirror symmetry is broken and the transition dipole along the ZZ direction becomes nonzero, as shown in

Fig. S5 in the Supplemental Material [34]. However, at 300 K, comparing to the AR direction, transition dipole moment in the ZZ direction is still four orders of magnitude smaller, which can be neglected in the absorption spectrum. Maybe at a higher temperature more interesting phenomena caused by broken symmetry can be observed.

Given the exciton energy and oscillator strength, we have all the information needed for absorption spectrum, which is calculated as below:

$$Abs(\omega) \propto \sum_{\lambda} T_{\lambda} \Gamma_L(\omega, \ E_{\lambda}, \ \sigma), \tag{2}$$

where $\Gamma_L(\omega, \ E_{\lambda}, \ \sigma)$ is the Lorentz function centered at the exciton energy E_{λ} with a broadening width σ set as 25 meV, T_{λ} the exciton oscillator strength, and λ the index of exciton state. Figure 4(f) shows several snapshots of absorption spectra at different moments along the AIMD trajectory. The location and the height of the peaks stay in fluctuation due to the lattice vibration. By averaging over the transient absorption spectra of the AIMD ensemble, we obtain the absorption spectrum at 300 K [Fig. 4(g)]. By fitting the first absorption peak using Lorentz function, it is found the peak width is extended to 52 meV, accompanying with a 68-meV redshift.

E. Exciton-phonon interaction on the exciton mobility

The acoustic phonon limited exciton mobility is evaluated using deformation potential method [42,43]. The carrier mobility is expressed as

$$\mu_i = \frac{e\hbar^3 \, C_{2D,i}}{k_B T m_i^* M^* E_{d,i}^2}, \tag{3}$$

where the subscript i denotes transport direction (x is AR, y is ZZ), T is the temperature, m_i^* the effective mass, and M^* is defined as $M^* = \sqrt{m_x^* m_y^*}$. The two-dimensional elastic modulus C_{2D} is calculated using $C_{2D} = 2\Delta_E/(S_0 \varepsilon^2)$ where ε is the normalized deformation, Δ_E the change of total ground-state energy of the system, and S_0 the lattice area in equilibrium. The deformation potential E_d is calculated using $E_d = \Delta_V/\varepsilon$, where Δ_V is the change of carrier energy under deformation. The exciton effective mass is approximately set to be the sum of electron and hole effective mass as given by the exciton hydrogen model, $m_{EXT}^* = m_e^* + m_h^*$ [44]. For every stretched or compressed structure of the primitive cell, an individual $GW + $ BSE is performed without the application of rigid dielectric function.

Figure 5 shows how the GW QP band gap and GW-BSE exciton energy change with lattice deformation. Table I lists the deformation potential, mobility, and other associated physical quantities of the electron, hole, and exciton at 300 K. Strikingly, the exciton mobility is $1 \sim 2$ orders lower than the mobility of uncorrelated electron or hole. According to Eq. (3), the mobility is inversely proportional to the square of effective mass and deformation potential. In addition to the hinderance caused by the combined effective mass, the transport of A exciton is also impeded by the combined deformation potential because the electron and hole energies have opposite changes upon phonon excitation. As one of the most famous members of the 2D material family, BP attracts wide and intense interest due to its high carrier mobility.
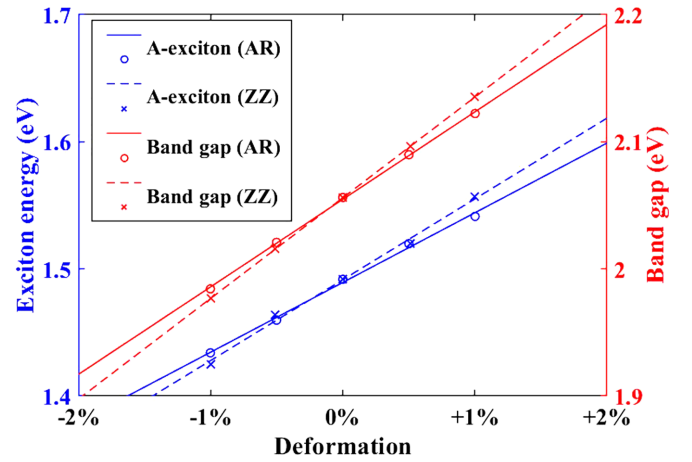

FIG. 5. *GW* band gap and energy of *A* exciton under different lattice deformation along AR direction (dots and solid lines) and ZZ direction (crosses and dashed lines) calculated by *GW* + BSE. Positive values of deformation correspond to tensile strain while negative values correspond to compressive strain. Dots (or crosses) represent calculated values and solid (or dashed) lines are linearly fitted curves.

Nevertheless, our study proposes that the carrier mobility will be dramatically suppressed if exciton is formed.

The strong anisotropic nature of MLBP is retained in the transport of exciton. The exciton mobility along the AR direction is an order larger than the ZZ direction owing to the huge difference of exciton effective mass in these directions. It should be noted that the electron holds large mobility in the AR direction, while the hole is highly mobile in the ZZ direction. The high hole mobility origins from that its small deformation potential overwhelms the heavy effective mass. However, this advantage is nullified when the hole and electron are combined together, possessing a relatively large deformation potential as a whole. Consequently, the anisotropy of exciton mobility follows the trend of electron. The exciton mobility along the ZZ direction is as small as $4.8 \, \text{cm}^2 \, \text{V} \, \text{s}^{-1}$ at 300 K, indicating that the exciton almost stays localized in this direction. This unique anisotropy leaves the transport of exciton in MLBP nearly one dimensional as revealed by the exciton-exciton annihilation experiments [25].

Figure 5 also illustrates the impact of lattice deformation on the exciton binding energy in MLBP. The slope of the band gap is larger than that of exciton binding in both AR and ZZ directions, implying the tensile strain will increase the exciton binding energy. As derived by the Thomas-Fermi

TABLE I. Effective mass (m^*), elastic modulus (C_{2D}), deformation potential (E_d), and mobility (μ) of exciton, electron, and hole at 300 K.

Carrier	Direction	m^*/m_e	C_{2D} (J/m²)	E_d (eV)	μ (cm² V s⁻¹)
Exciton	X	0.35	36.5	5.48 ± 0.06	45.8
	Y	7.64	112.6	6.36 ± 0.08	4.8
Electron	X	0.19	36.5	1.33 ± 0.02	5200
	Y	1.13	112.6	5.41 ± 0.01	159
Hole	X	0.16	36.5	4.01 ± 0.03	291
	Y	6.51	112.6	0.84 ± 0.05	508

model [45], the Coulomb screening is positively correlated to the electron density so that the stretched lattice under tensile strain weakens the screening effect and lifts up the binding energy. The acoustic mode has an essential influence on the binding energy—1% in-plane strain leads to about 15-meV change of binding energy, suggesting the potential of acoustic phonons as an effective approach to tune the binding behavior of excitons in MLBP.

In this work, the renormalization of the band gap and *ex-ph* effects on the exciton binding energy and wave function are investigated using the statistical sampling over the AIMD simulation, which can also be obtained using the perturbation theory [28,46]. If we compare the perturbation theory with the statistical-sampling approaches, both methods have their own advantages. One important problem of statistical-sampling approach is how to make a sufficient sampling. For example, AIMD with a sufficiently long time is required to obtain a complete ensemble. In addition, if AIMD simulation with periodic condition is applied to sample the phonon excitation, only the phonons at the Γ point are included. To overcome this problem, a supercell needs to be used so that the phonons at other q points in the primitive-cell Brillouin zone (BZ) can be folded into the Γ point of the supercell BZ. Therefore, the sampling of phonon q points is limited by the size of the supercell. For example, in this work, we use $6 \times 6 \times 1$ supercell, which can sample $6 \times 6 \times 1$ q points on the phonon dispersion curves. Another problem is that in the AIMD simulation, the nuclei are treated as classical particles, and the zero-point energy of the phonons are not included in the simulation. Using molecular dynamics methods based on path-integral techniques can solve this problem. On the other hand, the AIMD simulation can naturally capture the anharmonic effects of the phonons, which is an important advantage comparing to the perturbation theory.

IV. CONCLUSION

In summary, we have utilized GW + rtBSE method to study the *ex-ph* interaction in MLBP by exploring the evolution of exciton properties along the AIMD trajectory under room-temperature phonon excitation. It is found that A_g^2, A_g^1, and ZA modes have notable impacts on the exciton energy, and the exciton oscillator strength is highly susceptible to A_g^2 mode. The phonon excitation induces localization of A exciton along with 20-meV increase of binding energy and causes prominent redshift and broadening of absorption spectrum. Besides, based on the deformation potential theory we predict the exciton formation suppresses the carrier mobility by 1–2 orders of magnitude, and the anisotropic character of BP is kept for exciton mobility, featuring quasi-1D transport along the AR direction. The understanding of *ex-ph* interaction and exciton mobility at the *ab initio* level provides insights for designing and optimizing the high-performance 2D nanoelectronic devices based on BP in the future.

[1] L. Li, Y. Yu, G. J. Ye, Q. Ge, X. Ou, H. Wu, D. Feng, X. H. Chen, and Y. Zhang, Black phosphorus field-effect transistors, Nat. Nanotechnol. **9**, 372 (2014).

[2] L. Li, J. Kim, C. Jin, G. J. Ye, D. Y. Qiu, F. H. da Jornada, Z. Shi, L. Chen, Z. Zhang, F. Yang *et al.*, Direct observation of the layer-dependent electronic structure in phosphorene, Nat. Nanotechnol. **12**, 21 (2017).

[3] D. Y. Qiu, F. H. da Jornada, and S. G. Louie, Environmental screening effects in 2D materials: Renormalization of the bandgap, electronic structure, and optical spectra of few-layer black phosphorus, Nano Lett. **17**, 4706 (2017).

[4] G. Zhang, S. Huang, F. Wang, Q. Xing, C. Song, C. Wang, Y. Lei, M. Huang, and H. Yan, The optical conductivity of few-layer black phosphorus by infrared spectroscopy, Nat. Commun. **11**, 1847 (2020).

[5] G. Zhang, S. Huang, A. Chaves, C. Song, V. O. Özçelik, T. Low, and H. Yan, Infrared fingerprints of few-layer black phosphorus, Nat. Commun. **8**, 14071 (2017).

[6] F. Xia, H. Wang, and Y. Jia, Rediscovering black phosphorus as an anisotropic layered material for optoelectronics and electronics, Nat. Commun. **5**, 4458 (2014).

[7] S. Zhang, J. Yang, R. Xu, F. Yang, W. Li, M. Ghufran, Y. Zhang, Z. Yu, G. Zhang, Q. Qin, and Y. Lu, Extraordinary photoluminescence and strong temperature angle-dependent Raman responses in few-layer phosphorene, ACS Nano **8**, 9590 (2014).

[8] J. Qiao, X. Kong, Z.-X. Hu, F. Yang, and W. Ji, High-mobility transport anisotropy and linear dichroism in few-layer black phosphorus, Nat. Commun. **5**, 4475 (2014).

[9] V. Tran, R. Soklaski, Y. Liang, and L. Yang, Layer-controlled band gap and anisotropic excitons in few-layer black phosphorus, Phys. Rev. B **89**, 235319 (2014).

[10] X. Wang, A. M. Jones, K. L. Seyler, V. Tran, Y. Jia, H. Zhao, H. Wang, L. Yang, X. Xu, and F. Xia, Highly anisotropic and robust excitons in monolayer black phosphorus, Nat. Nanotechnol. **10**, 517 (2015).

[11] H. Liu, A. T. Neal, Z. Zhu, Z. Luo, X. Xu, D. Tománek, and P. D. Ye, Phosphorene: An unexplored 2D semiconductor with a high hole mobility, ACS Nano **8**, 4033 (2014).

[12] X. Peng, Q. Wei, and A. Copple, Strain-engineered direct-indirect band gap transition and its mechanism in two-dimensional phosphorene, Phys. Rev. B **90**, 085402 (2014).

[13] S. Huang, G. Zhang, F. Fan, C. Song, F. Wang, Q. Xing, C. Wang, H. Wu, and H. Yan, Strain-tunable van der Waals interactions in few-layer black phosphorus, Nat. Commun. **10**, 2447 (2019).

[14] N. Mao, X. Wang, Y. Lin, B. G. Sumpter, Q. Ji, T. Palacios, S. Huang, V. Meunier, M. S. Dresslhaus, W. A. Tisdale *et al.*, Direct observation of symmetry-dependent electron-phonon coupling in black phosphorus, J. Am. Chem. Soc. **141**, 18994 (2019).

[15] B. Liao, J. Zhou, B. Qiu, M. S. Dresselhaus, and G. Chen, Ab initio study of electron-phonon interaction in phosphorene, Phys. Rev. B **91**, 235419 (2015).

[16] X. Fan, G. Zhao, and S. Wang, Electron-phonon interaction and scattering in phosphorene, J. Phys. D: Appl. Phys. **51**, 155301 (2018).

[17] H. Guo, W. Chu, O. V. Prezhdo, Q. Zheng, and J. Zhao, Strong modulation of band gap, carrier mobility and lifetime in two-dimensional black phosphorene through electron-phonon coupling, J. Phys. Chem. Lett. **12**, 3960 (2021).

[18] R. Long, W. Fang, and A. V. Akimov, Nonradiative electron-hole recombination rate is greatly reduced by defects in monolayer black phosphorus: Ab initio time domain study, J. Phys. Chem. Lett. **7**, 653 (2016).

[19] L. Zhang, W. Chu, Q. Zheng, A. V. Benderskii, O. V. Prezhdo, and J. Zhao, Suppression of electron-hole recombination by intrinsic defects in 2D monoelemental material, J. Phys. Chem. Lett. **10**, 6151 (2019).

[20] H. Guo, W. Chu, Q. Zheng, and J. Zhao, Tuning the carrier lifetime in black phosphorene through family atom doping, J. Phys. Chem. Lett. **11**, 4662 (2020).

[21] Y. Yin, X. Zhao, X. Ren, K. Liu, J. Zhao, L. Zhang, and S. Li, Thickness dependent ultrafast charge transfer in BP/MoS$_2$ heterostructure, Adv. Funct. Mater. **32**, 2206952 (2022).

[22] V. Tran, R. Fei, and L. Yang, Quasiparticle energies, excitons, and optical spectra of few-layer black phosphorus, 2D Mater. **2**, 044014 (2015).

[23] J. He, D. He, Y. Wang, Q. Cui, M. Z. Bellus, H.-Y. Chiu, and H. Zhao, Exceptional and anisotropic transport properties of photocarriers in black phosphorus, ACS Nano **9**, 6436 (2015).

[24] A. Surrente, A. A. Mitioglu, K. Galkowski, L. Klopotowski, W. Tabis, B. Vignolle, D. K. Maude, and P. Plochocka, Onset of exciton-exciton annihilation in single-layer black phosphorus, Phys. Rev. B **94**, 075425 (2016).

[25] V. Pareek, J. Madéo, and K. M. Dani, Ultrafast control of the dimensionality of exciton-exciton annihilation in atomically thin black phosphorus, Phys. Rev. Lett. **124**, 057403 (2020).

[26] M. Zacharias and F. Giustino, Theory of the special displacement method for electronic structure calculations at finite temperature, Phys. Rev. Res. **2**, 013357 (2020).

[27] T. A. Huang, M. Zacharias, D. K. Lewis, F. Giustino, and S. Sharifzadeh, Exciton−phonon interactions in monolayer germanium selenide from first principles, J. Phys. Chem. Lett. **12**, 3802 (2021).

[28] H.-Y. Chen, D. Sangalli, and M. Bernardi, Exciton-phonon interaction and relaxation times from first principles, Phys. Rev. Lett. **125**, 107401 (2020).

[29] X. Jiang, Q. Zheng, Z. Lan, W. A. Saidi, X. Ren, and J. Zhao, Real-time GW-BSE investigations on spin-valley exciton dynamics in monolayer, Sci. Adv. **7**, eabf3759 (2021).

[30] G. Kresse and J. Furthmüller, Efficient iterative schemes for ab initio total-energy calculations using a plane-wave basis set, Phys. Rev. B **54**, 11169 (1996).

[31] J. P. Perdew, K. Burke, and M. Ernzerhof, Generalized gradient approximation made simple, Phys. Rev. Lett. **77**, 3865 (1996).

[32] S. Nosé, A unified formulation of the constant temperature molecular dynamics methods, J. Chem. Phys. **81**, 511 (1984).

[33] S. Ismail-Beigi and S. G. Louie, Excited-state forces within a first-principles green's function formalism, Phys. Rev. Lett. **90**, 076401 (2003).

[34] See Supplemental Material at http://link.aps.org/supplemental/10.1103/PhysRevB.108.245118 for the details of GW + rtBSE approach; comparison between absorption spectra calculated using VASP and HEFEI-NAMD; distribution of A exciton in the momentum space; CBM orbital repsonse to A_g^2 phonon mode excitation; transition dipole from VBM to CBM under ZZ polarization; and deformation potential of CBM electron and VBM hole.

[35] F. Giustino, S. G. Louie, and M. L. Cohen, Electron-phonon renormalization of the direct band gap of diamond, Phys. Rev. Lett. **105**, 265501 (2010).

[36] P. W. Anderson, Absence of diffusion in certain random lattices, Phys. Rev. **109**, 1492 (1958).

[37] E. Abrahams, P. W. Anderson, D. C. Licciardello, and T. V. Ramakrishnan, Scaling theory of localization: Absence of quantum diffusion in two dimensions, Phys. Rev. Lett. **42**, 673 (1979).

[38] M. M. Glazov, Z. A. Iakovlev, S. Refaely-Abramson, Phonon-induced exciton weak localization in two-dimensional semiconductors, Appl. Phys. Lett. **121**, 192106 (2022).

[39] A. M. Alvertis, J. B. Haber, E. A. Engel, S. Sharifzadeh, and J. B. Neaton, Phonon-induced localization of excitons in molecular crystals from first principles, Phys. Rev. Lett. **130**, 086401 (2023).

[40] S. Choi, J. Deslippe, R. B. Capaz, and S. G. Louie, An explicit formula for optical oscillator strength of excitons, Nano Lett. **13**, 54 (2013).

[41] M. Gajdoš, K. Hummer, G. Kresse, J. Furthmüller, and F. Bechstedt, Linear optical properties in the projector-augmented wave methodology, Phys. Rev. B **73**, 045112 (2006).

[42] F. S. Khan and P. B. Allen, Deformation potentials and electron-phonon scattering: Two new theorems, Phys. Rev. B **29**, 3341 (1984).

[43] J. Bardeen and W. Shockley, Deformation potentials and mobilities in non-polar crystals, Phys. Rev. **80**, 72 (1950).

[44] S. Helmrich, A. W. Achtstein, H. Ahmad, M. Kunz, B. Herzog, O. Schöps, U. Woggon, and N. Owschimikow, High phonon-limited mobility of charged and neutral excitons in mono- and bilayer MoTe$_2$, 2D Mater. **8**, 025019 (2021).

[45] N. W. Ashcroft, N. D. Mermin, and D. Wei, *Solid State Physics* (Cengage Learning, 2016).

[46] G. Antonius and S. G. Louie, Theory of exciton-phonon coupling, Phys. Rev. B **105**, 085111 (2022).